



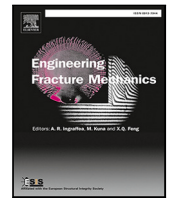
Numerical predictions of crack growth direction in a railhead under contact, bending and thermal loads

Downloaded from: <https://research.chalmers.se>, 2024-04-23 15:34 UTC

Citation for the original published paper (version of record):

Salahi Nezhad, M., Floros, D., Larsson, F. et al (2022). Numerical predictions of crack growth direction in a railhead under contact, bending and thermal loads. *Engineering Fracture Mechanics*, 261. <http://dx.doi.org/10.1016/j.engfracmech.2021.108218>

N.B. When citing this work, cite the original published paper.



Numerical predictions of crack growth direction in a railhead under contact, bending and thermal loads

Mohammad Salahi Nezhad ^{a,*}, Dimosthenis Floros ^b, Fredrik Larsson ^a, Elena Kabo ^c, Anders Ekberg ^c

^a Department of Industrial and Materials Science/CHARMEC, Chalmers University of Technology, SE 412 96 Gothenburg, Sweden

^b Volvo Cars, Gothenburg, Sweden

^c Department of Mechanics and Maritime Sciences/CHARMEC, Chalmers University of Technology, SE 412 96 Gothenburg, Sweden

ARTICLE INFO

Keywords:

Rolling contact fatigue
Crack growth direction
Crack propagation
Vector crack tip displacement

ABSTRACT

The effect of different operational loading scenarios on predicted crack growth direction for a propagating inclined railhead crack is assessed by 2D finite element simulations. Studied load scenarios include a moving Hertzian contact load, a temperature drop, rail bending due to a passing wheelset, and combinations thereof. The direction of the unbiased crack propagation is predicted using an accumulative vector crack tip displacement criterion. The numerical model is validated for the individual load scenarios. Restraints due to crack face locking are imposed by a threshold parameter, whose influence is also assessed. For combinations of thermal and contact loads, the predicted crack path is found to diverge gradually from transverse growth, corresponding to pure thermal loading, to shallow growth, corresponding to a pure contact load. For combined bending and contact loading, there is a discrete jump in the predicted crack direction as the contact load increased while the bending load is kept constant. These results are well aligned with empirical experience.

1. Introduction

Rolling contact fatigue (RCF) of railway wheels and rails is a pervasive, costly and complex phenomenon [1,2]. The most common form is surface initiated RCF, where cracks initiate at the surface and initially propagate at a shallow angle into the railhead. Cracks in wheels tend to deviate towards a growth angle that is (more or less) parallel to the surface after reaching a depth of some millimetres. As cracks merge, pieces of wheel tread material break off and cause pits. In an operational rail, the rolling contact load is acting in combination with longitudinal stresses due to rail bending and restricted thermal contraction/expansion of the continuously welded rail. Neither bending, nor the global thermal stresses are present in railway wheels. However, overheating and subsequent cooling may result in high tensile stresses at the wheel tread, see e.g. [3]. Due to these tensile stresses, transverse crack growth may occur in rails (and in overheated wheels). Transverse cracks in rails are expensive to mitigate and may cause rail breaks, which are obvious safety risks [4]. Specifically, transversely deviating surface initiated cracks are also hard to detect using common non-destructive testing techniques due to shielding effects of other shallower cracks [5]. Since not all railhead cracks deviate transversally, the ability to predict circumstances under which they do is crucial both from a safety and a maintenance perspective.

There are several criteria for mixed-mode fatigue crack growth predictions, as described in, e.g., [6]. However, RCF crack predictions are complicated by the fact that (frictional) rolling contact conditions cause a non-proportional multiaxial stress/strain

* Corresponding author.

E-mail addresses: salahi@chalmers.se (M. Salahi Nezhad), dimosthenis.floros@volvocars.com (D. Floros).

<https://doi.org/10.1016/j.engfracmech.2021.108218>

Received 22 July 2021; Received in revised form 23 December 2021; Accepted 28 December 2021

Available online 12 January 2022

0013-7944/© 2022 The Authors. Published by Elsevier Ltd. This is an open access article under the CC BY license

(<http://creativecommons.org/licenses/by/4.0/>).

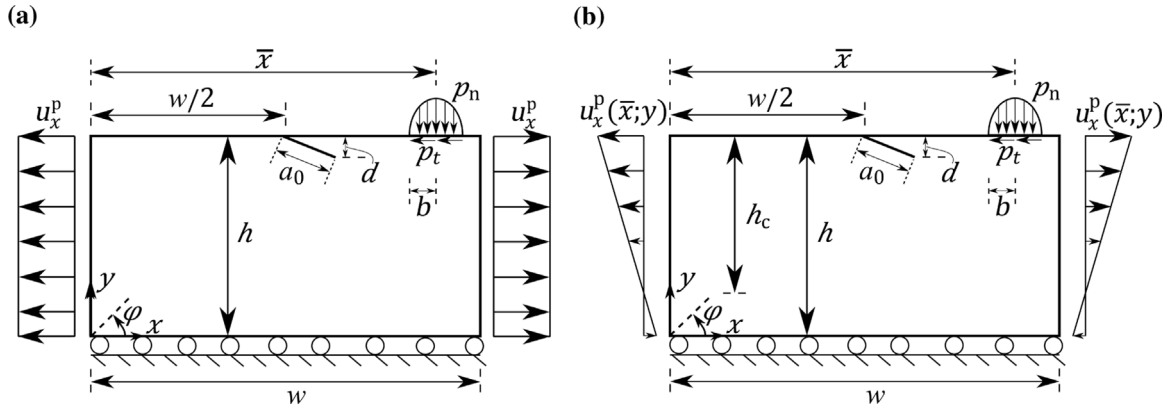


Fig. 1. Model of a 2D rail part with an inclined crack subjected to a Hertzian contact load (p_n, p_t) and, (a) constant longitudinal prescribed displacements u_x^p , or, (b) boundary displacements corresponding to bending $u_x^p(\bar{x}; y)$.

Table 1
Geometrical and material properties for the rail part depicted in Fig. 1.

w	300	mm,	h	100	mm
a_0	4.3	mm,	d	2.0	mm
E_r	210	GPa,	ν_r	0.3	–
E_w	199	GPa,	ν_w	0.3	–

state. This induces compression and mixed-mode deformations of RCF cracks. Thus, the majority of the currently available criteria in the literature for predicting fatigue crack growth direction are subjected to constraints that limit their predictive capabilities under non-proportional mixed-mode loading [7]. Stress intensity factor-based criteria such as maximum tangential stress criteria, see e.g. [8], are able to predict the crack path for cracks loaded mainly in tension. However, as shown in [9], they are inaccurate for shear-dominated growth. Maximum shear stress criteria predict shear driven growth accurately, but exhibit low accuracy for tensile-mode growth, see e.g. [9]. An energy-based criterion using configurational forces [9,10] was also used in [9], where it was shown that the performance of the criterion decreases as shear loading increases. The performance of the criterion is also sensitive to the material model used in the simulations and the approach for the evaluation of crack driving force (i.e. viscous or rate-independent), see [9]. In the same study, the Vector Crack Tip Displacement (VCTD) criterion yielded promising results in four fatigue tests simulated using a linear elastic material model [9]. It was also shown in [9] that modelling the cyclic elastic–plastic material response does not improve the accuracy of the predicted crack growth directions by VCTD. However, the criterion has not been investigated for operational loading conditions.

To be able to identify the operational conditions that cause transverse crack growth, a previously developed crack growth direction criterion in [9], expanded from [11] to account for non-proportional loading, is utilised in the current study. The criterion has previously been validated towards crack growth experiments featuring mixed-mode biaxial loading [9] and rolling contact loading [12]. However, the influence of thermal and bending loads in combination with contact loads has not been studied. In addition, the current study employs unbiased crack propagation in contrast to [12] where the tendency to follow (or deviate) from a predefined crack path was studied.

In the present work, Finite Element (FE) simulations with a 2D model of a rail part are carried out featuring an inclined surface-breaking crack. The rail section is subjected to a bending load, a passing contact load (contact pressure and wheel–rail friction) and a tensile load representing the thermal stress pertinent to a drop in temperature. In order to study different operational conditions, the load magnitudes are varied, and crack paths are predicted for both individual and combined loads. The critical loading conditions, which lead to the transverse growth, can be identified by comparing the crack paths for these loads.

The novelty of the research lies in the introduction of unbiased crack propagation, the analysis of crack growth under combined loading, the introduction of a restraint parameter to account for crack face locking and the assessment on its influence on the prediction.

2. Numerical model

2.1. Geometrical and material data

The geometrical and material properties of a rail section with an inclined crack are presented in Fig. 1 and in Table 1. Plane strain conditions are presumed and a linearly elastic material model is used for the rail part. The initial crack inclination is $\varphi_0 = -25^\circ$, which is a reasonable value for headcheck cracks [13,14]. The initial crack length is $a_0 = 4.3$ mm. In Table 1, E is the elastic modulus and ν indicates the Poisson's ratio. Subscripts r and w denote rail and wheel materials, respectively.

2.2. Loads and boundary conditions

Three load scenarios are investigated: contact loading due to the passage of a wheel along the top surface of the rail part, and longitudinal thermal and bending loading acting on the side edges of the rail part. As shown in Fig. 1, the bottom edge of the model is restrained in the global y -direction for all the load cases. For pure contact loading, both side edges of the model are clamped in the global x -direction ($u_x^p = 0$). Bending and thermal loads are transformed to corresponding longitudinal displacements ($u_x^p \neq 0$). The influence of each loading scenario on predicted crack path is evaluated independently and in combinations with the other scenarios. The load cases are detailed in the respective subsections.

2.2.1. Contact load

The contact pressure from a passing wheel is approximated using Hertzian contact theory [15]. The contact pressure distribution under 2D Hertzian conditions is assumed to follow an elliptic distribution [16]. More specifically, for a given contact load position \bar{x} , see Fig. 1a, the variation of the pressure along the top surface of the rail becomes

$$p_n(\bar{x}; x) = \begin{cases} \frac{2P}{\pi b^2} \sqrt{b^2 - [x - \bar{x}]^2} & |x - \bar{x}| < b \\ 0 & |x - \bar{x}| \geq b, \end{cases} \quad (1)$$

where P is the 2D contact load per unit thickness and $|\bullet|$ denotes absolute value. The semi-axis of the contact patch, b , corresponding to the contact load P is evaluated using

$$b = \sqrt{\frac{4PR}{\pi E^*}}, \quad (2)$$

where $R = 0.46$ m is the radius of the contacting cylinder (corresponding to the railway wheel), and E^* is the effective elastic modulus determined as

$$\frac{1}{E^*} = \frac{1 - \nu_r^2}{E_r} + \frac{1 - \nu_w^2}{E_w}. \quad (3)$$

In the evaluation of the wheel–rail frictional stress distribution, full slip conditions are presumed, $p_t(\bar{x}; x) = f_{wr} p_n(\bar{x}; x)$, where f_{wr} is the traction coefficient. To model the passage of a wheel over the rail in the simulations, the contact load is shifted in 100 increments along the top surface, from $\bar{x} = 0$ m to $\bar{x} = 0.3$ m. For load positions adjacent to the vertical boundaries, the part of the load falling outside the boundary is discarded. The majority of the considered load positions is located in the vicinity of the crack mouth where the influence on the crack tip deformation is the largest.

2.2.2. Thermal load

Presuming linear elasticity, the equivalent¹ thermal displacement at the edges for a rail section of length w is evaluated [17] as

$$u_x^p = -\alpha \Delta T \frac{w}{2}, \quad (4)$$

where $\alpha = 11.5 \times 10^{-6}$ [1/°C] is the thermal expansion coefficient of the rail material and $\Delta T = T - T_0$ [°C], is the temperature deviation from the stress-free temperature, T_0 .

In the simulations, the thermal load is applied as prescribed boundary displacements, u_x^p , according to Eq. (4), see Fig. 1a. During a load cycle, u_x^p is increased from zero to a peak value corresponding to the target temperature change and back to zero. In combined loading, the thermal load cycle is assumed to be much longer than the contact load cycle, that is, the temperature load is considered to be at its peak during the entire contact load passage.

2.2.3. Rail bending load

The bending moment in a rail due to a passing wheelset is evaluated using the in-house vertical dynamic vehicle–track interaction analysis code, DIFF [18]. To this aim, a 6 m track section with a distance between sleeper centres of 0.6 m is considered. Rail pad and ballast vertical stiffness values are set to 120 MN/m and 50 MN/m, respectively. It is presumed that the crack mouth is located at the midspan between two sleepers and that the rail has a 60E1 profile. A train with 7.5 t wheel load traverses the rail at a speed of 100 km/h. Fig. 2 shows the bending moment at the longitudinal position of the crack mouth for different wheel load positions.

Using the moment–curvature relation for an Euler–Bernoulli beam, the corresponding boundary displacements for a rail section of length w are obtained [17] as

$$u_x^p(\bar{x}; y) = \frac{M(\bar{x}) [y - [h - h_c]] w}{2E_r I_z}, \quad (5)$$

where $M(\bar{x})$ is the bending moment evaluated according to Fig. 2, I_z is the area moment of inertia of the rail profile and h_c is the distance between the top surface of the rail and the neutral axis of the rail cross-section. For a 60E1 rail profile, $I_z = 30.5 \times 10^{-6}$ m⁴ and $h_c = 0.091$ m [19]. In the simulations, $u_x^p(\bar{x}; y)$ is updated as the wheel load position \bar{x} changes, see Fig. 1b.

¹ The linear displacement field that reproduces the strain and stress fields in a uniform thermoelastic material confined in the x -direction.

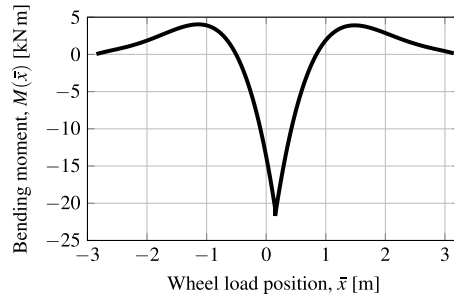


Fig. 2. Evolution of bending moment over time at the crack mouth due to a moving wheel load.

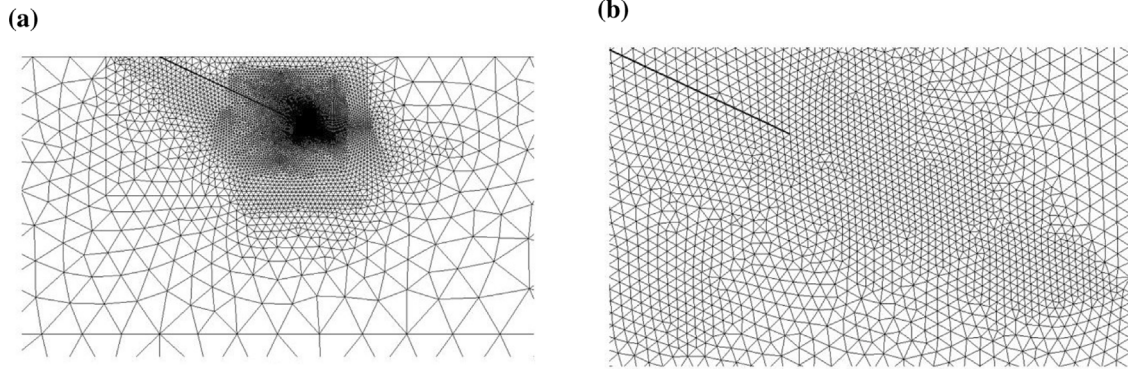


Fig. 3. FE mesh around the initial crack configuration. (a) Area around the crack. (b) Area around the crack tip.

3. Crack modelling and propagation criterion

The crack is modelled explicitly in the FE model via a discretisation that features two independent sets of nodes at the top and bottom surfaces of the crack (duplicate nodes). Three-noded triangular elements are employed for the entire mesh, which is refined close to the crack tip with element sizes down to $17\text{ }\mu\text{m}$, see Fig. 3. A penalty formulation is used to solve the normal contact problem between the crack faces, which are assumed frictionless. The latter is motivated by [12] where it was shown that crack face friction has a small effect on predicted directions.

3.1. Crack propagation criterion

In a local coordinate system with origin at the crack tip, see Fig. 4a, the fatigue crack growth direction with the original VCTD criterion [11] is determined as $\vartheta = \arcsin(\Delta\delta_{II}/\Delta\delta)$, where Δ denotes the range over a load cycle and $\Delta\delta = \sqrt{\Delta\delta_I^2 + 2\Delta\delta_I\Delta\delta_{II} + 2\Delta\delta_{II}^2}$. Here, δ_I and δ_{II} are the opening and sliding crack face displacements, respectively. These are determined at a predefined distance from the crack tip, d_h . To determine the direction of crack propagation for a load cycle, the VCTD criterion, as modified in [9] to account for out-of-phase loading, is implemented as follows:

1. $\delta_I(t)$ and $\delta_{II}(t)$ are computed at each time instance t of the load cycle at a constant d_h as

$$\delta_I(t) = [\mathbf{u}^+(t) - \mathbf{u}^-(t)] \cdot \hat{\mathbf{e}}_{\perp}, \quad \delta_{II}(t) = [\mathbf{u}^+(t) - \mathbf{u}^-(t)] \cdot \hat{\mathbf{e}}_{\parallel}, \quad (6)$$

where \mathbf{u}^+ and \mathbf{u}^- denote the displacements of adjacent points at the positive and negative sides of the crack, respectively, as shown in Fig. 4b. $\hat{\mathbf{e}}_{\parallel}$ and $\hat{\mathbf{e}}_{\perp}$ are the unit vectors in the parallel and perpendicular directions to the crack, respectively. In the current study, $d_h \approx 52\text{ }\mu\text{m}$ was used. For the FE-mesh in Fig. 3, this corresponds to slightly more than three times the element size at the crack tip.

2. The amplitudes of $\delta_I(t)$ and $\delta_{II}(t)$ are defined as

$$\tilde{\delta}_I(t) = \delta_I(t) - \bar{\delta}_I, \quad \tilde{\delta}_{II}(t) = \delta_{II}(t) - \bar{\delta}_{II}, \quad (7)$$

where $\bar{\delta}_I$ and $\bar{\delta}_{II}$ are mid values over a load cycle,

$$\bar{\delta}_I = \frac{1}{2} \left[\max_t (\delta_I(t)) + \min_t (\delta_I(t)) \right], \quad \bar{\delta}_{II} = \frac{1}{2} \left[\max_t (\delta_{II}(t)) + \min_t (\delta_{II}(t)) \right], \quad (8)$$

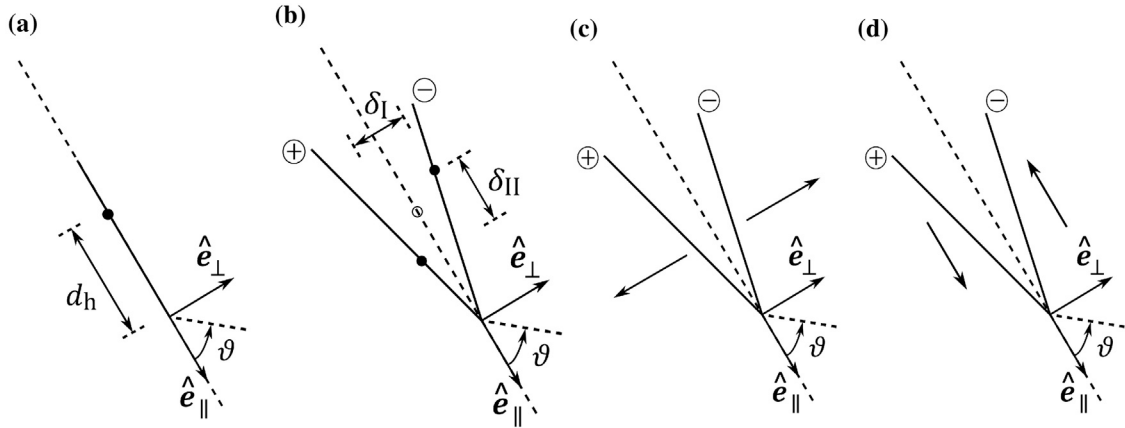


Fig. 4. Crack geometry configurations. A dashed line indicates the orientation of the undeformed crack. (a) Undeformed closed crack. (b) Crack tip displacements. (c) Illustration of positive δ_I . (d) Illustration of positive δ_{II} .

and, $\max(\bullet)$ and $\min(\bullet)$ indicate maximum and minimum over the load cycle. Amplitudes are here employed to reflect kinematic hardening effects due to local plasticity at the crack tip.

3. Following [11], the instantaneous crack driving displacement is defined as

$$\tilde{\delta}(t) = \sqrt{\langle \tilde{\delta}_I(t) \rangle^2 + 2\langle \tilde{\delta}_I(t) \rangle \langle \tilde{\delta}_{II}(t) \rangle + 2\tilde{\delta}_{II}(t)^2}, \quad (9)$$

where $\langle \bullet \rangle$ are the Macaulay brackets, $\langle \bullet \rangle = [\bullet + |\bullet|]/2$. The instantaneous crack growth direction is determined as

$$\vartheta(t) = \arcsin \frac{\tilde{\delta}_{II}(t)}{\tilde{\delta}(t)}, \quad (10)$$

where $\vartheta(t)$ is expressed in the local coordinate system of Fig. 4a.

4. The crack driving displacement for the entire load cycle is determined by

$$\Delta \mathbf{a} = \underset{\Delta \mathbf{a} \in \{\Delta \mathbf{a}^+, \Delta \mathbf{a}^-\}}{\operatorname{argmax}} \|\Delta \mathbf{a}\|, \quad (11)$$

where $\|\bullet\|$ is the Euclidean norm and $\{\Delta \mathbf{a}^+, \Delta \mathbf{a}^-\}$ is the set of trial crack driving displacements for presumed positive and negative growth directions defined as

$$\Delta \mathbf{a}^+ = \int_0^{T_c} \delta \mathbf{a}^+(t) dt, \quad \delta \mathbf{a}^+(t) = \langle d_t \tilde{\delta}(t) \rangle \hat{\mathbf{e}}_\vartheta(t) f^+(t), \quad (12)$$

$$\Delta \mathbf{a}^- = \int_0^{T_c} \delta \mathbf{a}^-(t) dt, \quad \delta \mathbf{a}^-(t) = \langle d_t \tilde{\delta}(t) \rangle \hat{\mathbf{e}}_\vartheta(t) f^-(t), \quad (13)$$

where $\delta \mathbf{a}^+(t)$ and $\delta \mathbf{a}^-(t)$ are the instantaneous trial crack driving displacements for presumed positive and negative growth directions, respectively, T_c is the length of the load cycle and $d_t \tilde{\delta}(t_n) = \tilde{\delta}(t_n) - \tilde{\delta}(t_{n-1})$. Furthermore, $\hat{\mathbf{e}}_\vartheta$ is the instantaneous unit vector in the direction of $\vartheta(t)$ determined from Eq. (10), and

$$f^+(t) = \begin{cases} 0 & \tilde{\delta}_{II} < 0 \text{ and } \frac{\delta_I}{|\delta_{II}|} \leq \psi \\ 1 & \tilde{\delta}_{II} \geq 0 \text{ or } \frac{\delta_I}{|\delta_{II}|} > \psi \end{cases}, \quad f^-(t) = \begin{cases} 0 & \tilde{\delta}_{II} > 0 \text{ and } \frac{\delta_I}{|\delta_{II}|} \leq \psi \\ 1 & \tilde{\delta}_{II} \leq 0 \text{ or } \frac{\delta_I}{|\delta_{II}|} > \psi, \end{cases} \quad (14)$$

where ψ is the reversed shear threshold parameter defined below.

5. The growth direction ϕ predicted for the entire load cycle in the local coordinate system of Fig. 4a is defined by its unit vector,

$$\hat{\mathbf{e}}_\phi = \frac{\Delta \mathbf{a}}{\|\Delta \mathbf{a}\|}. \quad (15)$$

The reversed shear threshold parameter, ψ , is used to account for crack face locking by restricting the contribution of reversed shear instances according to Eq. (14). Here, crack face locking is defined as in [20] meaning that a part of the crack is active at each time instant. For inactive part(s) of the crack, there are no relative displacements between the closed crack faces. Also, ‘‘Reversed shear’’ refers to a shear deformation with the opposite sign to the presumed growth direction. It can be noted that $\psi < 0$ would impose no restrictions on reversed shear contribution and equal contributions in two opposite shear directions during a load cycle would cancel each other out. Setting $\psi = 0$ imposes restrictions on reverse shear when there is active contact, while $\psi > 0$ requires crack opening to allow for reversed shear. In the current study, $\psi = 0.001$ was used, unless otherwise stated.

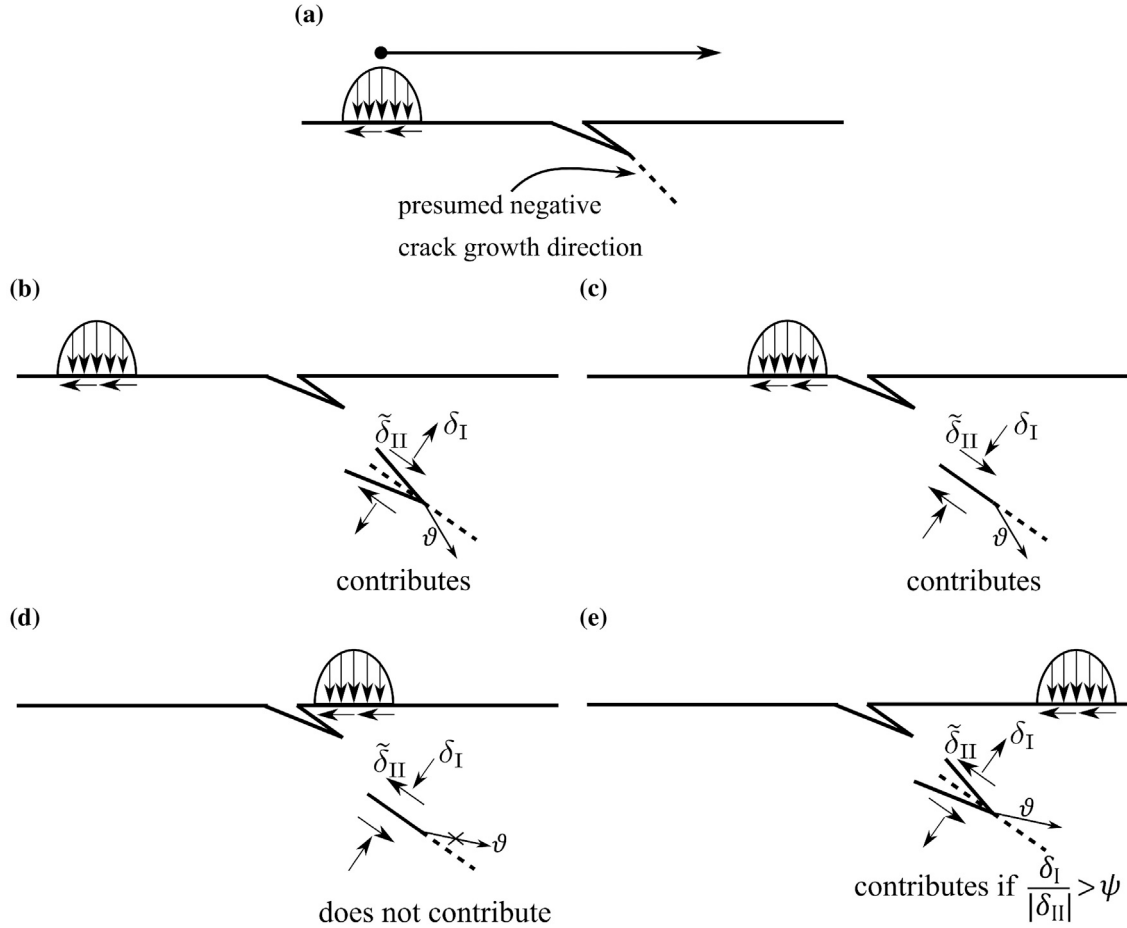


Fig. 5. Contribution to the $\Delta a^-(t)$ at different contact load positions illustrated for a load case with substantial wheel–rail traction. A dashed line indicates the orientation of the undeformed crack. (a) Initial load and crack setup. (b) Open crack with a negative $\tilde{\delta}_{II}$. (c) Closed crack with a negative $\tilde{\delta}_{II}$. (d) Closed crack with a positive $\tilde{\delta}_{II}$. (e) Open crack with a positive $\tilde{\delta}_{II}$.

The effect of ψ in preventing reversed shear contribution for closed cracks is illustrated in Fig. 5, where the contribution to the trial crack driving displacement for presumed negative growth, $\Delta a^-(t)$, at four different contact load positions is investigated using evaluated values of $f^-(t)$. As seen in Fig. 5, $\tilde{\delta}_{II}$ is negative for load positions (b) and (c), thus $f^-(t) = 1$, that is, these load positions contribute to $\Delta a^-(t)$. At contact load position (d), $f^-(t)$ does not contribute to $\Delta a^-(t)$, since $\tilde{\delta}_{II}$ is positive and the condition, $\delta_I/|\delta_{II}| > \psi$, is not fulfilled due to crack closure. For contact load position (e), $\tilde{\delta}_{II}$ is positive. However, since the crack is open, $\delta_I/|\delta_{II}| > \psi$ may be fulfilled and $f^-(t)$ will in that case contribute to $\Delta a^-(t)$.

4. Analyses and results

The 2D FE-model of the rail part with an embedded surface-breaking crack described in Section 2.1 was implemented in Abaqus CAE [21]. The model was subjected to the load scenarios detailed in Section 2.2, individually or in combinations. The modified VCTD criterion outlined in Section 3.1 was implemented in a MATLAB [22] function for unbiased prediction of the direction of crack growth. In the analyses, the crack was propagated a small distance in the predicted direction, whereby crack deformations in the subsequent load cycle were analysed. The analyses thus featured “incrementally” stationary cracks, i.e. no growth during the load cycle was considered. Predicted crack growth angles, ϕ , were expressed in the global coordinate system of Fig. 1a, φ , using $\varphi = \varphi_0 + \phi$. The maximum crack face penetration obtained in the analyses was on the order of $10^{-8} - 10^{-7}$ m (depending on the load type), which is considered acceptable.

4.1. Individual load cases

4.1.1. Contact load

Simulations featuring a moving 2D Hertzian contact load, in accordance with Section 2.2.1, were carried out with the model depicted in Fig. 1a for $u_x^p = 0$. The magnitude of the contact load was $P = 33.8$ MN/m, whereby the semi-axis of the contact patch

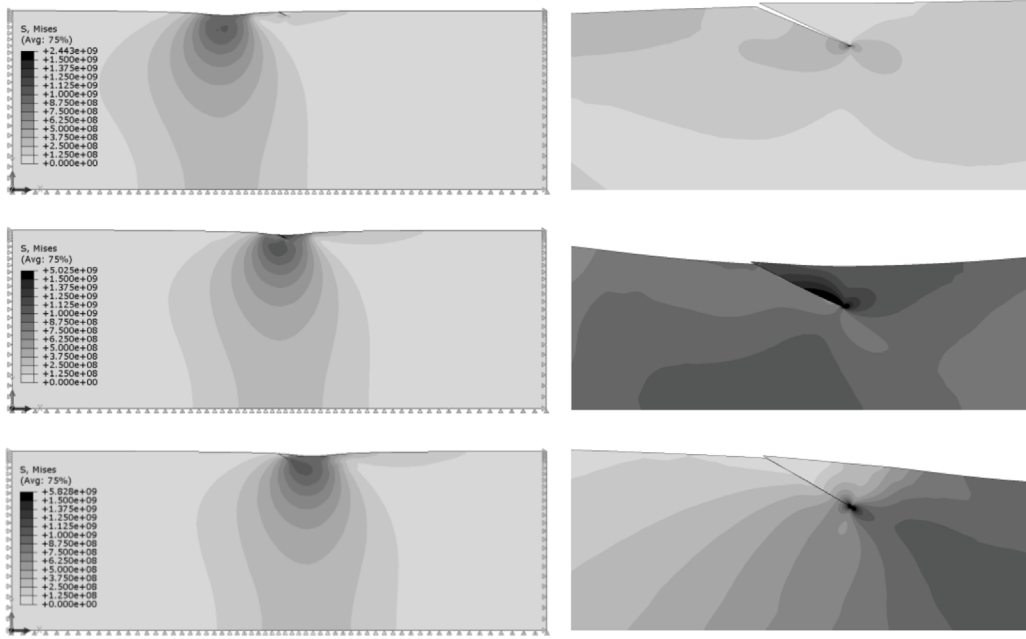


Fig. 6. Von Mises stress distribution for the initial crack under pure contact load for three load positions before (top), at (middle) and after (bottom) the crack (deformation scale factor = 10). To the left are the distributions for the global model and to the right magnified images around the crack tip are presented.

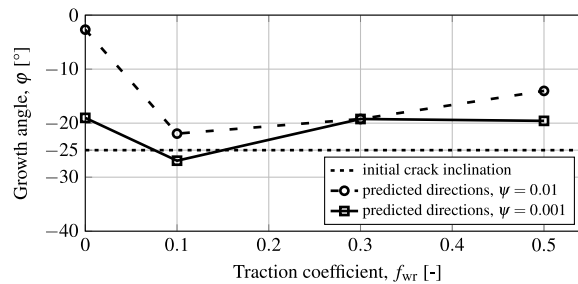


Fig. 7. Predicted crack growth directions for the initial crack subjected to a contact load of 33.8 MN/m.

from Eq. (2) became $b = 13.3$ mm. As an illustration, for this particular loading, the von Mises effective stress distribution is presented in Fig. 6 for a sequence of load positions. Similar to the findings in [23] for subsurface defects, the moving contact load leads to a rotating stress state around the crack tip.

Predicted crack growth angles, φ , for the initial crack configuration subjected to rolling contact loads with varying wheel-rail traction coefficients, f_{wr} , are presented in Fig. 7. Results are shown for reversed shear threshold parameter $\psi = 0.001$ and $\psi = 0.01$. Based on results from simulations of twin-disc experiments [12], it is expected that the crack propagates at a shallow angle to the surface of the rail under pure contact load. The overall trend of the depicted curves in Fig. 7 is thus as expected. The only exception is the case of $f_{wr} = 0$ and $\psi = 0.01$, which is investigated further below.

The instantaneous growth angle expressed in terms of the global coordinate system of Fig. 1a, $\varphi_{inst}(t)$, using $\varphi_{inst}(t) = \varphi_0 + \vartheta(t)$, where $\vartheta(t)$ was determined by Eq. (10), and, $\|\delta a^-(t)\|$, evaluated from Eq. (13), are provided in Fig. 8 for the first load cycle. The presence of instantaneous crack driving displacements around $\bar{x} = 0.165$ m for $\psi = 0.001$ is observed. This constitutes a reversed shear loading, as indicated by the change of sign in φ_{inst} . This contribution is suppressed for $\psi = 0.01$, since the crack opening is not large enough to fulfil $\delta_I/|\delta_{II}| > \psi$. This causes the outlier result for the case of $f_{wr} = 0$ and $\psi = 0.01$.

4.1.2. Thermal loading

Prescribed longitudinal displacements, u_x^p , according to Eq. (4) with $\Delta T = -20$ °C were employed to impose a pure thermal load ($P = 0$ MN/m) on the FE-model of Fig. 1a, in accordance with Section 2.2.2. Imposed crack growth increments at the end of each load cycle were initially set to 0.5 mm in the growth direction. Based on empirical observations, the crack is expected to propagate in mode I, perpendicular to the uniaxial tensile loading. As seen in Fig. 9a, the predicted crack paths reflect this assumption. For the thermal load, results are not sensitive to the ψ value since $\delta_I > 0$ at all time instances. To investigate the effect of the increment

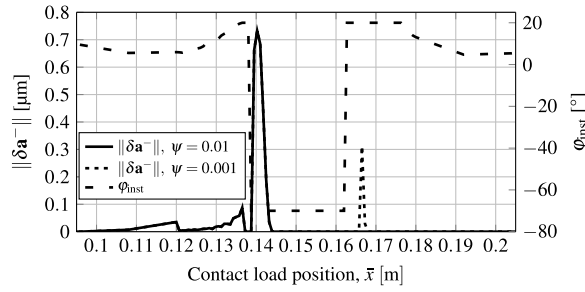


Fig. 8. Instantaneous growth angle expressed in the global coordinate system of Fig. 1a, ϕ_{inst} , and, trial crack driving displacements for presumed negative growth, $\|\delta a^-(t)\|$, for $\psi = 0.01$ and $\psi = 0.001$, for the first contact load cycle with $f_{\text{wr}} = 0$.

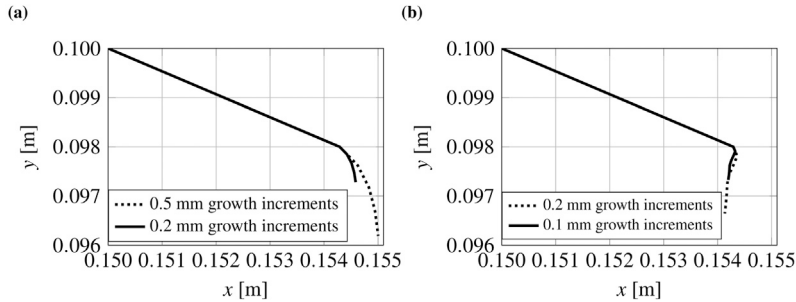


Fig. 9. Predicted crack propagation paths for variable crack growth increment sizes in the same FE-mesh. (a) Thermal loading and (b) Bending loading.

size on the predicted crack path, growth increments were reduced to 0.2 mm. This resulted in a convergence to mode I propagation after the same number of growth increments. Thus, it is concluded that the converged crack growth direction is not sensitive to the growth increment size, whereas it is dependent on the number of propagation increments.

4.1.3. Rail bending

Crack growth investigations under a pure bending load (i.e. $P = 0$) with the model depicted in Fig. 1b were performed. Boundary displacements corresponding to the bending moment in Fig. 2 were evaluated using Eq. (5). Growth increments of 0.2 mm in the direction of propagation were considered. The bending load subjects the crack mainly to mode I deformation, however with a large compressive phase that induces significant shear on an inclined crack. As seen in Fig. 9b, the crack is predicted to have a mode I dominated propagation path, which is considered reasonable. The crack path tends to pass -90° and then deviate back to a fairly transverse direction. This behaviour could be due to the influence of the larger compressive loads, exceeding the tensile loads. Hence, there may be an additional influence of shear driven growth. It can be compared to the usually diagonal (i.e. shear driven) growth that can be seen for cracks in the web of rails, see e.g. [24]. In that location the shear stress due to bending is higher and the normal stress is lower than for our studied case, which explains the larger influence of the shear stress. Similarly to the case of the pure thermal load, the bending load results are not sensitive to the ψ value. Reducing the crack growth increment size to 0.1 mm resulted in a crack path featuring the same trend as that for 0.2 mm, cf. Fig. 9b.

A comparison between the obtained responses to the (uniform) thermal load and the bending load, indicates that the large compression in the bending load induces an “instability” in the convergence of the predicted propagation angle. The predicted crack path also becomes more “jagged” in comparison to the growth path corresponding to the thermal load.

In order to evaluate the effect of mesh size on crack path predictions, a sensitivity analysis was performed on three different FE-discretisations for bending load analyses. The analyses featured the initial mesh (see Fig. 3) consisting of 20 044 degrees-of-freedom (DOF), a coarse mesh (12 520 DOF), and a fine mesh (58 444 DOF). The same value for d_h was used for all the studied FE-meshes. Results for three growth increments are shown in Fig. 10. It is observed that the predicted crack paths are almost identical. Thereby, it can be concluded that the employed mesh is sufficiently fine.

4.2. Combined load cases

4.2.1. Combinations of thermal and contact loads

The model in Fig. 1a was loaded by boundary displacements u_x^p corresponding to a thermal load of $\Delta T = -20^\circ\text{C}$, and by moving Hertzian contact loads with magnitudes of $P = 7.3\text{ MN/m}$ and $P = 33.8\text{ MN/m}$. The traction coefficient was set to $f_{\text{wr}} = 0.3$.

The predicted crack paths after three 0.2 mm growth increments for the studied load combinations are depicted in Fig. 11 for $\psi = 0.001$ and $\psi = 0.01$. It is seen that a decrease in the contact load magnitude increases the tendency for deviation towards a more

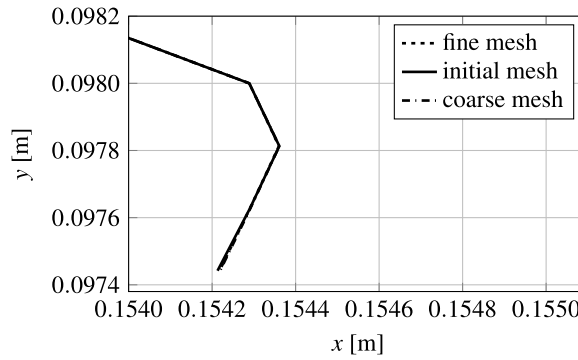


Fig. 10. Zoom-in of predicted crack propagation paths for different FE-meshes (case of pure bending load).

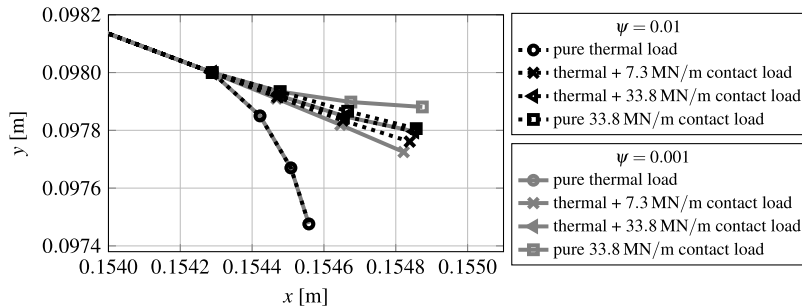


Fig. 11. Predicted crack propagation paths for combinations of contact and thermal loads.

transverse growth. This deviation takes place gradually and is caused by the increased influence of the thermal (tensile) loading,² which keeps the crack open and promotes mode I growth.

4.2.2. Combined bending and contact load

The model in Fig. 1b was subjected to the boundary displacements corresponding to the bending moment in Fig. 2, and a 2D contact load with varying load magnitudes, P , ranging from 3.0 MN/m to 33.8 MN/m with a traction coefficient of $f_{\text{wr}} = 0.3$. Predictions were made for reversed shear threshold parameter $\psi = 0.001$ and $\psi = 0.01$.

The predicted crack growth directions for the initial crack are presented in Fig. 12. It is seen that for low contact loads the crack tends to grow in a similar direction as for a pure bending load. As the contact load increases, the predicted direction deviates towards a direction corresponding to a pure contact load. The transition between the two predicted growth directions is sharp at a transition contact load magnitude. For $\psi = 0.001$, the transition occurs at a lower contact load magnitude than for $\psi = 0.01$ and the shear driven growth is in a direction closer to the initial crack inclination (-25°). This is because in the case of $\psi = 0.001$, more time instances in reversed shear contribute to the total propagation of the crack during a load cycle.

The predicted crack paths after three 0.2 mm growth increments for different load combinations are illustrated in Fig. 13 for $\psi = 0.01$. It is observed that bending and low contact loads result in crack path predictions similar to those of pure bending, whereas the predicted crack paths for larger contact loads combined with bending are closer to the crack path for a pure contact load. Additional simulations (not shown here) show that the trends are almost identical between $\psi = 0.001$ and $\psi = 0.01$, however, the jump between the dominating directions occurs at a lower contact load for $\psi = 0.001$, as also seen in Fig. 12.

5. Conclusions and outlook

A robust tool for simulating RCF crack propagation in a linear elastic material has been developed and implemented in a 2D model of a rail with a surface-breaking inclined crack. An accumulative VCTD criterion has been employed to predict crack growth direction in unbiased (i.e. not following a prescribed path) analyses. To account for crack face locking, a threshold parameter has been introduced to impose restrictions on crack growth in the case of a reversed shear crack loading. The predictions have been validated against analyses featuring a previously validated in-house code [12] for a moving Hertzian contact load, and qualitatively validated for the thermal and bending loads; for a purely tensile load cycle, the crack deviated into mode I growth as expected. In

² Since only the direction of growth is estimated in the current study, it is the ratio between the contact and thermal loads that is of influence.

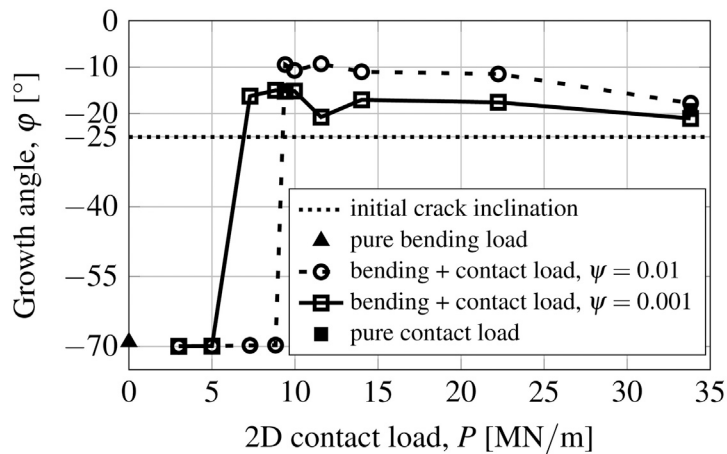


Fig. 12. Predicted crack growth directions for the initial crack under combinations of bending and contact load.

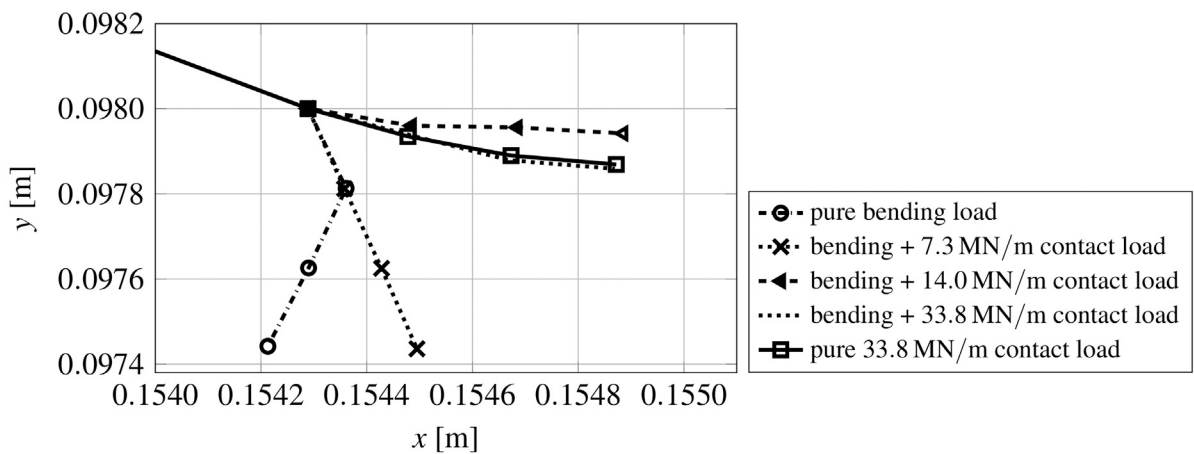


Fig. 13. Predicted crack propagation paths for combinations of bending and contact loads for $\psi = 0.01$.

cyclic bending, corresponding to operational conditions for a railhead crack with a compressive peak stress about four times higher than the tensile peak stress, the crack deviated towards a direction close to mode I growth.

The effects of the moving Hertzian contact load in combination with thermal or bending load were investigated. Combined thermal and contact loads resulted in a predicted crack path that gradually shifted from transverse growth (under pure thermal loading), to shallow growth (pure contact load). For combinations of bending and contact loads, the same trend was found, with the exception that the predicted crack path changes abruptly as the contact load exceeds a certain magnitude. However, it is not possible to quantify the operational wheel–rail contact load that corresponds to this transition due to the 2D approximation. It was also found that the combined effect of large compression due to bending and the contact stress as the contact load passes near the crack mouth, in some cases, can lead to predicted crack propagation directions that are shallower than for the pure contact load. These analyses of combined operational loading agree well with the empirical experience of cracks that either propagate at a shallow trajectory, or deviate to transverse growth[25].

For all studied load cases, the predicted crack propagation direction under the unbiased simulation converged with the number of load cycles towards a (more or less distinct) final direction. The development of the crack growth direction depended on the number of propagation increments, but was almost insensitive to the size of the growth increment. Predicted crack paths for pure contact load, and for combinations of bending and contact loads, were found to be sensitive to the employed value of the reversed shear threshold parameter.

For future studies, additional load combinations will allow to draw more precise conclusions regarding the influence of different loads on predicted RCF crack paths. Moreover, a further sensitivity analysis on loading and predictive model parameters will increase the understanding of sensitivities and limitations of the numerical model. By having a robust tool for predicting growth directions, the loading (i.e. the contribution to each mode) of propagating cracks will be easier to evaluate and then the challenge of predicting growth rates for the out-of-phase mixed-mode loaded cracks can be addressed.

Further, a crack in a 3D rail should be investigated. A significant challenge here (in addition to computational demands) is that the crack may propagate in different directions in each position along the crack front.

CRedit authorship contribution statement

Mohammad Salahi Nezhad: Conceptualization, Methodology, Software, Validation, Writing – original draft, Writing – review & editing. **Dimosthenis Floros:** Conceptualization, Methodology, Software, Writing – review & editing. **Fredrik Larsson:** Resources, Validation, Writing – review & editing. **Elena Kabo:** Resources, Validation, Writing – review & editing. **Anders Ekberg:** Resources, Validation, Writing – review & editing.

Declaration of competing interest

The authors declare that they have no known competing financial interests or personal relationships that could have appeared to influence the work reported in this paper.

Acknowledgements

The current study is part of the ongoing activities in CHARMEC – Chalmers Railway Mechanics (www.chalmers.se/charmec). Parts of the study have been funded from the European Union's Horizon 2020 research and innovation programme in the projects In2Track2 and In2Track3 under grant agreements Nos 826255 and 101012456.

References

- [1] Magel EE. Rolling contact fatigue: A comprehensive review. US Department of Transportation, Federal Railroad Administration; 2011. <http://dx.doi.org/10.4224/23000318>.
- [2] Ekberg A, Kabo E. Fatigue of railway wheels and rails under rolling contact and thermal loading—an overview. *Wear* 2005;258(7):1288–300. <http://dx.doi.org/10.1016/j.wear.2004.03.039>.
- [3] Esmaeili A, Walia MS, Handa K, Ikeuchi K, Ekh M, Vernersson T, et al. A methodology to predict thermomechanical cracking of railway wheel treads: From experiments to numerical predictions. *Int J Fatigue* 2017;105:71–85. <http://dx.doi.org/10.1016/j.ijfatigue.2017.08.003>.
- [4] Smith RA. The wheel–rail interface—some recent accidents. *Fatigue Fract Eng Mater Struct* 2003;26(10):901–7. <http://dx.doi.org/10.1046/j.1460-2695.2003.00701.x>.
- [5] Magel E, Mutton P, Ekberg A, Kapoor A. Rolling contact fatigue, wear and broken rail derailments. *Wear* 2016;366–367:249–57. <http://dx.doi.org/10.1016/j.wear.2016.06.009>.
- [6] Rozumek D, Macha E. A survey of failure criteria and parameters in mixed-mode fatigue crack growth. *Mater Sci* 2009;45:190. <http://dx.doi.org/10.1007/s11003-009-9179-2>.
- [7] Zerres P, Vormwald M. Review of fatigue crack growth under non-proportional mixed-mode loading. *Int J Fatigue* 2014;58:75–83. <http://dx.doi.org/10.1016/j.ijfatigue.2013.04.001>.
- [8] Dahlin P, Olsson M. The effect of plasticity on incipient mixed-mode fatigue crack growth. *Fatigue Fract Eng Mater Struct* 2003;26(7):577–88. <http://dx.doi.org/10.1046/j.1460-2695.2003.00622.x>.
- [9] Floros D, Ekberg A, Larsson F. Evaluation of crack growth direction criteria on mixed-mode fatigue crack growth experiments. *Int J Fatigue* 2019;129:105075. <http://dx.doi.org/10.1016/j.ijfatigue.2019.04.013>.
- [10] Runesson K, Larsson F, Steinmann P. On energetic changes due to configurational motion of standard continua. *Int J Solids Struct* 2009;46(6):1464–75. <http://dx.doi.org/10.1016/j.ijsolstr.2008.11.011>.
- [11] Li C. Vector CTD criterion applied to mixed mode fatigue crack growth. *Fatigue Fract Eng Mater Struct* 1989;12(1):59–65. <http://dx.doi.org/10.1111/j.1460-2695.1989.tb00508.x>.
- [12] Floros D, Ekberg A, Larsson F. Evaluation of mixed-mode crack growth direction criteria under rolling contact conditions. *Wear* 2020;448–449:203184. <http://dx.doi.org/10.1016/j.wear.2020.203184>.
- [13] Heyder R, Girsch G. Testing of HSH® rails in high-speed tracks to minimise rail damage. *Wear* 2005;258(7):1014–21. <http://dx.doi.org/10.1016/j.wear.2004.03.050>.
- [14] Stock R, Pippin R. RCF and wear in theory and practice—The influence of rail grade on wear and RCF. *Wear* 2011;271(1):125–33. <http://dx.doi.org/10.1016/j.wear.2010.10.015>.
- [15] Hertz H. Ueber die Berührung fester elastischer Körper. *J Reine Angew Math* 1882;92:156–71.
- [16] Johnson KL. Contact mechanics. Cambridge University Press; 1985. <http://dx.doi.org/10.1017/CBO9781139171731>.
- [17] Timoshenko SP, Goodier JN. *Theory of Elasticity*. McGraw-Hill; 1951.
- [18] Nielsen JCO, Igeland A. Vertical dynamic interaction between train and track influence of wheel and track imperfections. *J Sound Vib* 1995;187(5):825–39. <http://dx.doi.org/10.1006/jsvi.1995.0566>.
- [19] CEN. Railway applications. track. rail. vignole railway rails 46 kg/m and above. EN 13674-1:2011, European Committee for Standardization; 2011.
- [20] Lansler E, Kabo E. Subsurface crack face displacements in railway wheels. *Wear* 2005;258(7):1038–47. <http://dx.doi.org/10.1016/j.wear.2004.03.053>.
- [21] ABAQUS/Standard user's manual, version 2020. Dassault Systèmes Simulia Corp.; 2020.
- [22] MATLAB 9.7.0.1190202 (R2019b). The MathWorks Inc.; 2019.
- [23] Kabo E. Material defects in rolling contact fatigue — influence of overloads and defect clusters. *Int J Fatigue* 2002;24(8):887–94. [http://dx.doi.org/10.1016/S0142-1123\(01\)00193-1](http://dx.doi.org/10.1016/S0142-1123(01)00193-1).
- [24] UIC leaflet 712: Rail defects. International Union of Railways (UIC); 2018.
- [25] Ekberg A, Åkesson B, Kabo E. Wheel/rail rolling contact fatigue – Probe, predict, prevent. *Wear* 2014;314(1–2):2–12. <http://dx.doi.org/10.1016/j.wear.2013.12.004>.